SIMULATING LASER PULSE PROPAGATION UNDER OPTIMIZED CONDITIONS FOR HIGH-HARMONIC GENERATION

by

Matthew D. Turner

A senior thesis submitted to the faculty of

Brigham Young University

in partial fulfillment of the requirements for the degree of

Bachelor of Science

Department of Physics and Astronomy

Brigham Young University

August 2007

BRIGHAM YOUNG UNIVERSITY

DEPARTMENT APPROVAL

of a senior thesis submitted by

Matthew D. Turner

This thesis has been reviewed by the research advisor, research coordinator, and department chair and has been found to be satisfactory.

Date	Justin B. Peatross, Advisor
Date	Eric Hintz, Research Coordinator
Date	Ross L. Spencer, Chair

ABSTRACT

SIMULATING LASER PULSE PROPAGATION UNDER OPTIMIZED CONDITIONS FOR HIGH-HARMONIC GENERATION

Matthew D. Turner

Department of Physics and Astronomy

Bachelor of Science

We numerically simulate the propagation of a high-intensity laser pulse to investigate the role of nonlinear effects in our high-harmonics generation experiments. The model uses an approximation of the nonlinear wave equation, which includes the Kerr effect and plasma generation, to model the evolution of an electric field envelope as it propagates through the region of interest. The initial condition for the field is calculated from Fresnel integrals to decrease computation time and include the effects of a aperture located before the focusing lens.

Numerical results for the radial fluence profile, fluence full-width at half-maximum, spectral shift, and ionization levels agree very well with previous experimental results. Removal of the nonlinear effects from the propagation code shows that the Kerr effect has a negligible influence in our setup. The simulations demonstrate that plasma generation is responsible for an observed

double focus in the fluence.

ACKNOWLEDGMENTS

I would first like to thank my wife for her love and support while I have worked on this project. I would also like to thank my parents for their support over the years. I am especially grateful to Dr. Peatross for the direction, instruction, and financial support he has provided while I have worked in his group. A number of other students in our group have also helped me and made long days in the lab tolerable. This work was partially supported by NSF grant PHY-0457316.

Contents

List of Figures

Chapter 1

Introduction

1.1 High-Harmonic Generation

First observed in 1987 by McPherson *et al.* [1], laser high-harmonic generation can occur when a high-intensity laser pulse interacts with the outer electrons of atoms to produce radiation of a shorter wavelength, as depicted in Fig. 1.1. The output radiation has frequencies that are odd multiples of the frequency of the input ($\lambda_{harmonic} = \lambda_{laser}/q$, where q is an odd integer), is coherent (*i.e*, a highly directional beam), and has a linear polarization matching that of the input beam. The spectrum of the generated output often reaches into the extreme ultraviolet (EUV), with wavelengths ranging down to a few nanometers. Because EUV light is quickly absorbed by most substances, the harmonics must propagate in a vacuum after generation if they are to be used or measured.

High-harmonic generation is being investigated as a source of useful EUV radiation for various applications. Computer chip production relies on photolithography, which is limited by the wavelength of the light used to expose the photoresist. Using EUV radiation would allow for much smaller circuit traces than those possible with visible

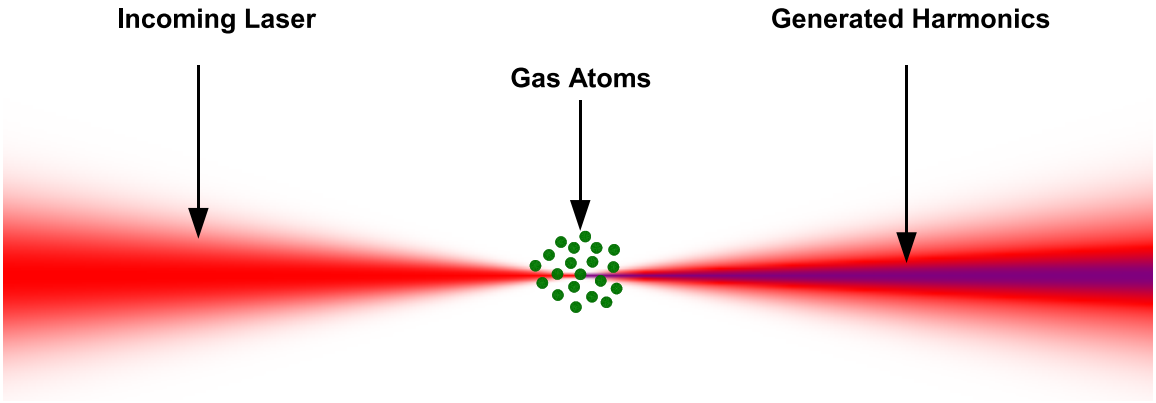

Figure 1.1 High-harmonics are generated by focusing a high-intensity laser pulse into a noble gas.

and near-visible UV light. A characterized and controllable source of EUV light is also needed for the testing of EUV optics, which are used in astronomical observations and in EUV lithography. Other sources of EUV light are synchrotron beam lines and laser-generated plasmas. High-harmonic generation fills a gap between these two types of sources, as it is much more economical than a synchrotron and provides more versatility than a plasma source by offering a greater spectral range and controllable polarization. Although the power output of high-harmonic generation is much too low for use in lithographic applications, it is well suited for testing EUV optics. A polarimeter employing high-harmonic generation as its source of EUV light has recently been constructed at Brigham Young University [2].

1.2 Phase Matching

High-harmonics are generated by an interaction between the electric field of the incoming laser pulse and the valence electrons of the atoms being used (typically a noble gas). The phase of the harmonics depends on the phase of the laser pulse at the point of generation. Slight spatial variations in the phase of the incoming

pulse can therefore translate into large variations in the phase of the harmonics, as $\phi_{\text{harmonics}} = q\,\phi_{\text{laser}}$. These large variations can result in destructive interference of the generated light, diminishing the amount of high-harmonic output. Phase variations are inevitable, due to the Gouy shift, intensity-dependent phase variation, and the high-intensity phenomena of the Kerr effect and plasma generation [3]. All of these sources of phase variation can combine to result in low conversion efficiencies.

1.3 Previous Work at BYU

In 1997, Prof. Peatross's group, proposed using counterpropagating laser pulses to disrupt the generation of harmonics in specific regions of the laser focus [4]. This technique uses counterpropagating light that is much weaker than the main pulse to eliminate harmonic generation in selected regions. The use of a counter-propagating pulse also provides a method for probing the extent of the region where harmonics are generated [3]. For her master's thesis, Julia Sutherland determined that the length of the high-harmonic generation region in helium was on the order of 1 cm in our setup, much longer than expected [3]. The group also found that inserting an aperture before the focusing lens, as shown in Fig. 1.2, boosts harmonic output in our setup by over an order of magnitude, much more than other groups have observed [5–8].

For his masters thesis, John Painter measured the spatial profile of the laser pulse in the BYU setup. The pulse passes through an 9 mm aperture before the focusing mirror, which optimized the harmonic output. Measurements of the beam width in the region of the focus provided what was initially thought to be direct evidence of filamentation, as explained in the next section. Fig. 1.3 shows data collected in the beam focus region for beam propagation under vacuum and in 80 torr of helium. The latter case shows a dual focus, with the beam narrowing, enlarging, and narrowing

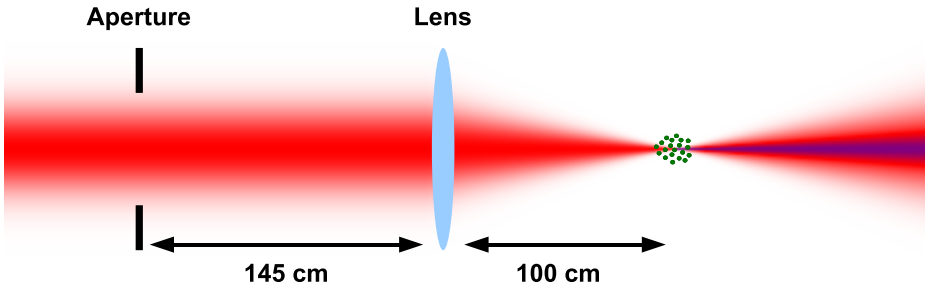

Figure 1.2 Variation of the diameter of an aperture on an incoming laser pulse was shown by Sutherland *et al.* to influence high-harmonic generation efficiencies.

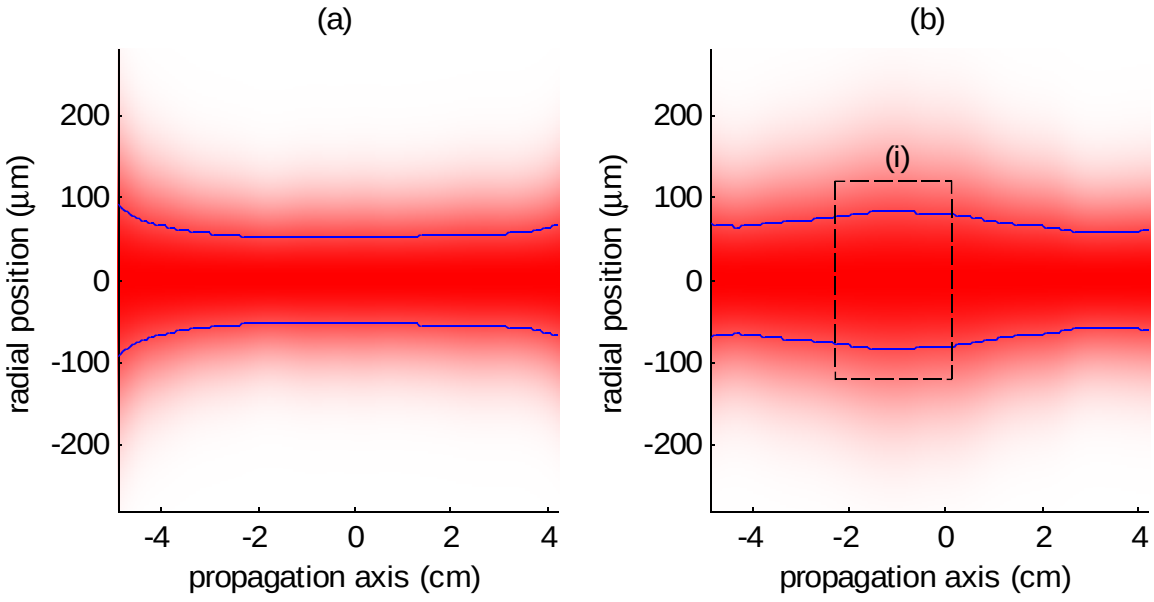

Figure 1.3 Experimental beam-width data showing the beam profile (red) and half-maximum (blue) for (a) propagation in vacuum and (b) propagation in 80 torr of Helium. Region (i) is the area of optimal harmonic generation [9].

again before finally spreading after the focal region. This phenomenon is due to nonlinear effects and is investigated numerically in this thesis. The area between the two foci was also found to be the region of brightest harmonic generation.

1.4 Nonlinear Index and Self-focusing

There are two nonlinear effects that play important roles in the propagation of high-intensity pulses. One is the Kerr effect, which is an intensity-dependent correction to the index of refraction of the medium, as given in

$$n = n_0 + n_2 I, \tag{1.1}$$

where n is the effective index of refraction, n_0 is the usual index, n_2 is the Kerr index, and I is the intensity of the propagating light at the point of interest. In the case of a high-intensity beam or pulse, the increase in the optical index in the more intense regions can cause an effect of self-focusing.

The second nonlinear effect of interest is rapid plasma generation and the resultant change to the index of refraction. As the pulse passes through the gas, electrons are ionized from of the atoms by the strong electric field. Some of the electrons are smashed back into their parent atom, resulting in harmonic generation, but many atoms remain ionized. The presence of these ionized atoms, or plasma, creates a frequency-dependent index of refraction according to

$$\eta_{plasma} = \sqrt{1 - \frac{\omega_p^2}{\omega^2}}, \tag{1.2}$$

where ω_p, the plasma frequency, is given by

$$\omega_p^2 = \frac{q_e^2 N}{m_e \epsilon_0} \tag{1.3}$$

with N, q_e, and m_e being the electron density, charge, and mass, respectively. This change to the optical index results in a defocusing effect.

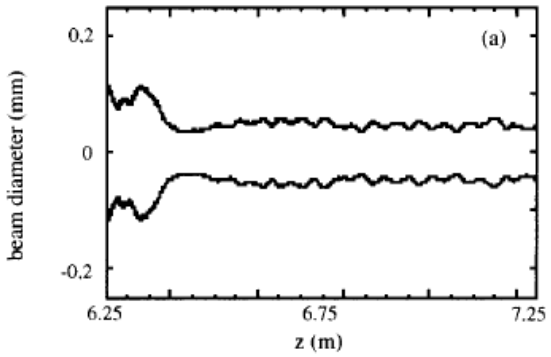

Figure 1.4 An example of filamentation taken from Chiron *et al.* [11]

.

When both the Kerr effect and plasma generation are present, filamentation can occur. Filamentation is a phenomenon resulting from the interplay of the self-focusing effect of the Kerr index and the defocusing effect of plasma generation, as exemplified in Fig. 1.4. As the pulse first nears the focus, the Kerr effect causes increased focusing, raising the peak intensity. The higher on-axis intensity increases the plasma frequency, defocusing the light and lowering the rate of plasma generation. This allows the Kerr effect to again dominate, focusing the light again. The process repeats until sufficient energy is lost to prevent self-focusing. The interplay between the two effects sometimes lasts for distances much larger than the Rayleigh range before before the pulse finally spreads. Filaments have been observed in air with lengths over 300 m [10]. When we saw the double-focusing in our earlier laser measurements, we suspected this type of Kerr-style focusing. However, as will be demonstrated in this thesis, the Kerr nonlinear index is not needed to explain our observations. This agrees with the expectation that the Kerr index is negligible for our gas density and peak power.

1.5 Nonlinear Simulations

Many groups have used numerical simulations to model high-intensity pulse propagation [7, 12–20]. Most have investigated long-range filamentation in air, but others have performed similar simulations in other media, including noble gases. The primary focus of these simulations, however, has been to investigate long-range filamentation and the behavior of optical pulses at higher intensities, without addressing the issue of high-harmonic generation. A limited number of groups have numerically investigated high-harmonic generation, with both one-dimensional models [5] and three-dimensional models [21–24].

Some groups have used models to investigate the role of beam geometry on the optimization of on-axis harmonic output [5, 6]. We have found no literature, however, reporting on the use of an apertured pulse as the initial condition for a three-dimensional simulation. The one paper that does mention using an apertured pulse as the initial condition of a three-dimensional simulation only roughly approximates the pulse geometry by means of a modified Gaussian pulse [24], which fails to account for diffraction effects caused by the aperture.

1.6 Overview

Although many groups working on high-harmonic generation accept the beneficial effects of a prefocus aperture, only a few groups have done theoretical work to investigate how an aperture can improve harmonic generation efficiencies. To study this effect, I developed a numerical code to simulate an apertured pulse and to propagate it with both linear and nonlinear effects. This code, as will be detailed in the Chapter 2, uses the Crank-Nicolson method to numerically solve the nonlinear paraxial slowly-varying wave equation beginning with an initial condition generated by Fres-

nel integrals. The results of the simulation, as given in Chapter 3, agree with our experimental measurements of the pulse profile, spectral shift, and losses of energy to ionization. It also explains the dual-focusing seen in Fig. 1.3, a major accomplishment of this project. The code can be used to investigate phase-matching zones within the pulse and determine optimal experimental setup parameters.

Chapter 2

Numerical Methods

This chapter provides the theoretical background and an overview of the numerical methods used to simulate the propagation of a high-intensity laser pulse through a gas. The numerical code presented here is based on the scheme presented by Chiron *et al.* in 1999 [11], which was developed to model pulse propagation in air. Matlab® was used to both run the propagation code and create graphical representations of the results.

2.1 The Wave Equation

To construct the numerical scheme for our simulation, we begin with the inhomogeneous scalar wave equation

$$\nabla^2\mathcal{E} - \frac{1}{c^2}\frac{\partial^2\mathcal{E}}{\partial t^2} = \frac{\omega^2}{c^2}(1-n^2)\mathcal{E}, \tag{2.1}$$

where $\mathcal{E}$ is the scalar electric field. When the pulse length is much longer than a wavelength, a slowly-varying-envelope approximation (SVEA) may be used. The field of a wave packet is represented by a plane wave multiplied by a time-dependent

complex scalar spatial envelope E:

$$\mathcal{E}(\mathbf{r},t) = E(\mathbf{r},t)e^{i(k_0 z-\omega_0 t)}. \tag{2.2}$$

Inserting (2.2) into (2.1), dividing out the exponential term, and assuming $\partial^2 E/\partial t^2 \ll (2i\omega_0)\partial E/\partial t$ (*i.e.*, the features of E are much larger than the wavelength associated with ω_0) results in the SVEA form of the wave equation:

$$\nabla^2 E(\mathbf{r},t) + 2ik_0\frac{\partial E(\mathbf{r},t)}{\partial z} + \frac{2i\omega_0}{c^2}\frac{\partial E(\mathbf{r},t)}{\partial t} = \frac{\omega_0^2}{c^2}(1-n^2)E. \tag{2.3}$$

Assuming radial symmetry eliminates the azimuthal term of the Laplacian. The paraxial approximation of $\partial^2 E/\partial z^2 \ll 2ik_0\partial E/\partial z$ eliminates the axial term, resulting in the paraxial SVEA wave equation:

$$\nabla_r^2 E(\mathbf{r},t) + 2ik_0\frac{\partial E(\mathbf{r},t)}{\partial z} + \frac{2i\omega_0}{c^2}\frac{\partial E(\mathbf{r},t)}{\partial t} = \frac{\omega_0^2}{c^2}(1-n^2)E. \tag{2.4}$$

The index of refraction n has two parts, the usual index of refraction n_0, and the nonlinear adjustment Δn. Assuming that $n_0^2 \approx 1$ and $\Delta n^2 \ll 2n_0\Delta n$,

$$\nabla_r^2 E(\mathbf{r},t) + 2ik_0\frac{\partial E(\mathbf{r},t)}{\partial z} + \frac{2i\omega_0}{c^2}\frac{\partial E(\mathbf{r},t)}{\partial t} + 2\frac{\omega_0^2}{c^2}n_0\Delta n E = 0. \tag{2.5}$$

(A derivation of the last nonlinear term in Eq. (2.5) is also given in Ref. [25].) The nonlinear change to the optical index contains two terms involving the local intensity, I, and the local plasma frequency, ω_p:

$$\Delta n = n_2 I - \frac{\omega_p^2}{2\omega_0^2}. \tag{2.6}$$

Using a numerical method to solve (2.5) directly would present a problem–solving this equation with sufficient resolution for the entire region of interest would require an enormous amount of memory and processing power. In order to circumvent these problems, a conventional technique substitutes scaled moving-frame variables for the variables in the equation [11, 26]. Substituting $\eta = z/(c/\omega_0)$, $\tau = \omega_0 t - \eta\omega_0/(k_0 c)$,

and $\rho = r/(c/\omega_0)$ into Eq. (2.5) eliminates units from the equation, normalizes magnitudes, and puts the equation into a frame that moves along the axis of propagation at the same speed as the pulse. The coordinate τ is called the the local time and η is the propagation distance. The substitution results in the final form that I used for my numerical computation:

$$\frac{2ik_0c}{\omega_0}\frac{\partial E}{\partial \eta} + \nabla_\rho^2 E + 2n_0\Delta n E = 0 \tag{2.7}$$

2.2 Differentiation Scheme

To solve (2.7) I employed the Crank-Nicolson differentiation scheme. The Crank-Nicolson method is implicit and is inherently stable [27]. It has been used for comparable simulations by other groups. One problem with using the Crank-Nicolson scheme, however, comes from the nonlinear term in the equation. The Crank-Nicolson scheme solves implicitly by averaging in time when calculating spatial derivatives, using linear algebra to include the future values in the calculations. Although the future value of a nonlinear term cannot be included in such calculations, the current value can be included. If variation in the nonlinear index over time is sufficiently small, *i.e.* $\Delta n(\rho, \tau, \eta + \Delta\eta) \approx \Delta n(\rho, \tau, \eta)$, the present value can be used alone instead of averaging it with the future value. Using this approximation, the resulting numerical scheme is

$$\begin{aligned} &E_{N,M}\left(p_+ - \frac{i\Delta\xi}{4}\Delta\epsilon\right) - \eta_1\left[(1+u_M)\,E_{N,M+1} + (1-u_M)\,E_{N,M-1}\right] \\ &= E_{N-1,M}\left(p_- + \frac{i\Delta\xi}{4}\Delta\epsilon\right) + \eta_1\left[(1+u_M)\,E_{N-1,M+1} + (1-u_M)\,E_{N-1,M-1}\right], \end{aligned} \tag{2.8}$$

with $\eta_1 = i\Delta\xi/(4\Delta\rho^2)$, $\Delta\xi = \Delta\eta/n_0$, $p_\pm = 1 \pm 2\eta_1$, $u_M = 1/[2(M-1)]$, and $\Delta\epsilon = 2n_0\Delta n$, where N is the step value along the axis of propagation and M is the radial step value. This is identical to the numerical equation of Chiron *et al.* [11],

except for an extra factor of 1/2 in the $i\Delta\xi/4$ terms. (This error causes a propagated pulse to focus twice as quickly as it should.) For the points where $\rho = 0$, the first term in (2.7) is undefined; however, the substitution

$$\lim_{\rho\to 0} \nabla_\rho^2 E = 2\frac{\partial^2 E}{\partial \rho^2} \quad \text{when } \frac{\partial E}{\partial \rho} = 0, \tag{2.9}$$

can be made, which, because of radial symmetry, is valid at all on-axis points. Since the simulation is radially symmetric, it can be performed in the range $\rho \geq 0$, halving the number of points. The second derivative at $\rho = 0$, which would otherwise depend on the values at $\rho = 0$, $\rho = -\Delta\rho$, and $\rho = \Delta\rho$, can be calculated solely from $\rho = 0$ and $\rho = \Delta\rho$.

2.3 Kerr Effect

If a simulated pulse has a sufficiently high peak power and no nonlinear effects other than Kerr self-focusing are present, the pulse will collapse to a mathematical singularity after a certain distance. The critical power can be calculated by the formula [25]

$$P_c = \frac{3.77\lambda^2}{8 n_0 n_2}. \tag{2.10}$$

To verify that my simulation of the Kerr effect was correct, I propagated pulses with varying peak powers, checking that that a pulse collapses only when it has a peak power equal to or greater than the critical value. Figs. 2.1 and 2.2 show the results for four of these simulations, with no Kerr effect, $P_{\max} = 0.5P_c$, $P_{\max} = 0.9P_c$ and $P_{\max} = P_c$. The simulations show that the Kerr effect does affect propagation at subcritical peak powers by moving the focus forward and tightening the profile, but collapse does not occur until the critical power is reached. This confirms that the simulation of the Kerr effect in my code agrees with theory.

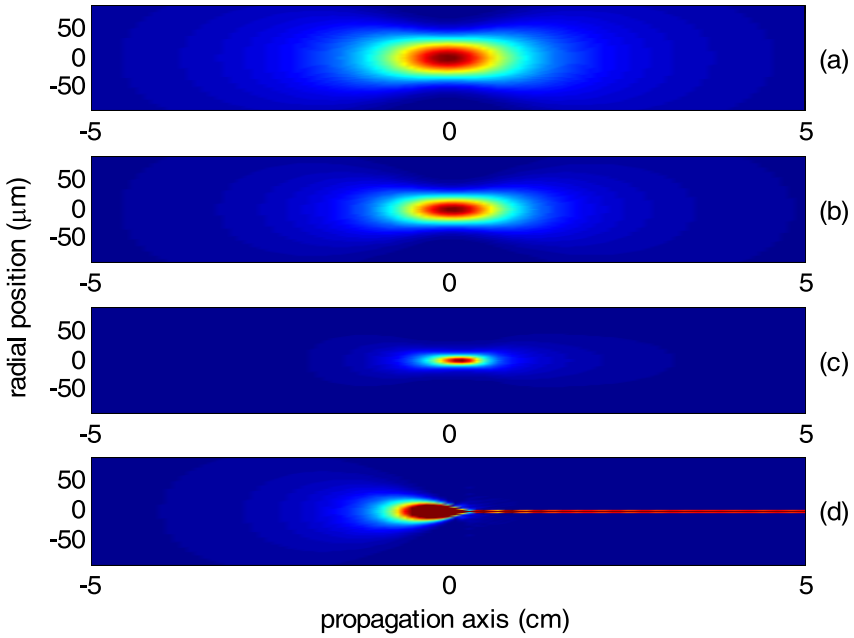

Figure 2.1 Beam intensity profiles for four cases: (a) no Kerr effect, (b) $P_{\max} = .5P_c$, (c) $P_{\max} = .9P_c$, and (d) $P_{\max} = P_c$. Scaling is relative to the peak intensity in each subfigure, except in (d) where the high postcollapse intensity would make the precollapse region invisible.

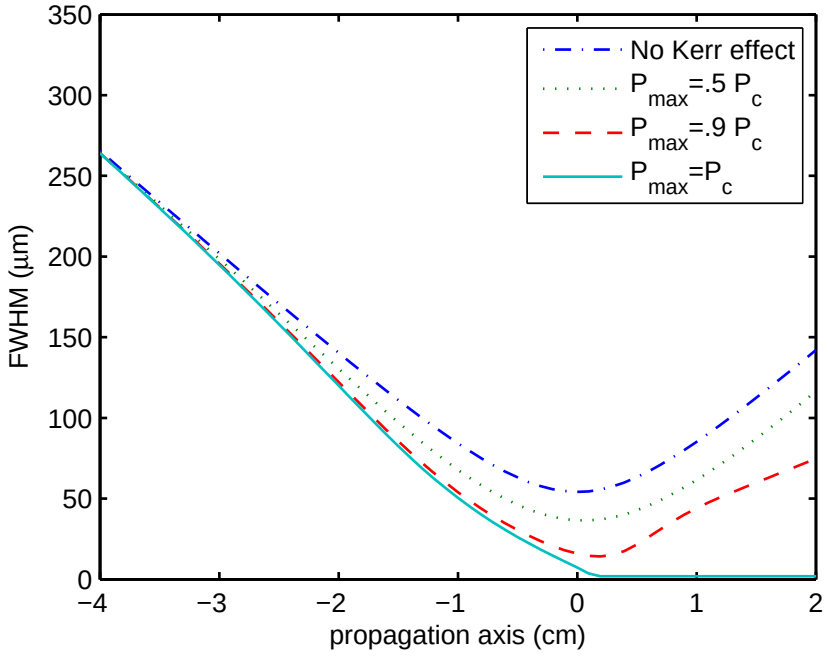

Figure 2.2 FWHM profiles for the four cases shown in Fig. 2.1.

2.4 Plasma Generation

The plasma generation segment of the simulation is based on the Ammosov-Delone-Krainov (ADK) model of tunneling ionization [28]. In order to calculate the change in the index of refraction due to plasma generation as given in (2.6), the density of free electrons N_e in each cell must be calculated. This is done in each step for each point by integrating the ionization rate $w(\tau')$ over local time from the beginning of the pulse to the current point:

$$\frac{n_e(\tau)}{n_{\text{total}}} = 1 - \exp\left(-\int_{-\infty}^{\tau} w(\tau')d\tau'\right). \tag{2.11}$$

If the pulse variation between each time step is small, this method is valid and obviates the needs to both track the electron density throughout the whole propagation region and limit the propagation step size to the length of the cells, dramatically reducing the calculation time.

Using the electron density, the plasma frequency is given by the equation

$$\omega_p^2 = \frac{N_e(\tau) q_e^2}{m_e \epsilon_0}. \tag{2.12}$$

where q_e and m_e are the electron charge and mass, and ϵ_0 is the permittivity of free space. The Kerr index n_2 is also influenced by plasma generation. As atoms are ionized, the density of the gas reduces and n_2 reduces proportionally:

$$n_{2\text{-effective}} = (1 - \frac{N_\text{e}}{N_\text{total}}) n_2. \tag{2.13}$$

2.5 Verification of Propagation Calculations

Propagation of a Gaussian pulse as described in Section 2.3 served as a check for errors in the simulation code. By comparing the result to the analytical solution for a Gaussian beam and monitoring conservation of energy, the amount of error could be determined. A pulse was propagated without nonlinear effects from $z = -5$ cm to $z = 5$ cm in a window with a radius of 20 times the beam waist w_0, 512 radial points, and a propagation step size $\Delta z = 125\,\mu$m. The intensity of the result differed from the Gaussian beam by a maximum $< 0.5\%$. Energy, as obtained for each frame by integrating in space and time, varied by $< 0.01\%$. These results show that this window is large enough to prevent the creation of boundary artifacts and that the step size is small enough for a valid approximation of the propagation derivative. In simulations involving the Kerr effect and plasma generation, comparison with an analytical solution is not possible, but pulse energy can still be monitored and is conserved to within .01%.

2.6 Using an Apertured Laser Beam for the Initial Condition

An important motivation for performing this simulation was to investigate the role of an aperture on the incoming pulse, as shown in Fig. 1.2. Simply propagating a pulse through the aperture and lens to the focal region would be much too demanding computationally, so I instead generate the initial condition for the propagation code at a short distance before the focal region. To do this, I wrote code to perform two sequential Fresnel integrals of the form

$$E(\rho, z=d) = -\frac{2\pi i e^{ikd} e^{i\frac{k\rho^2}{2d}}}{\lambda d} \int_{\text{aperture}} \rho' d\rho' E(\rho', z=0)\, e^{i\frac{k\rho'^2}{2d}} J_0\left(\frac{k\rho\rho'}{d}\right) \tag{2.14}$$

where $z = 0$ is the location of the aperture. In accordance with our beam setup (Fig. 1.2), the code first uses a Gaussian profile at an aperture to calculate the field at the lens. This field is then multiplied by $exp(-i\frac{k}{2f}\rho^2)$, the phase shift due to a lens of focal length f, and another Fresnel integral is performed to calculate the field of the initial condition region. In order to create a pulse with the proper curvature, a spatial envelope of the form $exp(-(R-R_0)^2/l^2)$ is applied to the field, where l is the pulse length, R_0 is the radius of curvature at the center of the pulse as given by $R_0 = z_{\text{center}} + z_0^2/z_{\text{center}}$ with z_0 as the Rayleigh range, z_{center} as the longitudinal position of the center of the pulse, and $R = \sqrt{(z + z_0^2/z_{\text{center}})^2 + r^2}$ is the distance to the center of curvature, where z is the longitudinal position of the current point. The numerical calculation of the fresnel integral was verified by calculating the on-axis field strength for a plane wave diffracting through a single aperture and comparing it to the analytical solution.

Chapter 3

Results and Conclusion

This chapter describes the application of the propagation code from Chapter 2 to simulate our experimental setup. During each simulation run, the code stores a specified number of snapshots of the electric field, intensity, and ionization, which are saved to a file along with the parameters of the propagation. An auxiliary program uses these snapshots to analyze the pulse propagation and to create graphical representations of the data: a fluence (energy/area) profile, fluence full-width at half-maximum (FWHM) measurements, peak intensities, total energy, and spectral content. Fluence, rather than intensity, is used to calculate the beam width, since our detection system measures total energy captured. The simulation results, using the parameters and geometry of our laser system, agree with and explain the experimental measurements obtained by our group [9].

3.1 Comparison with Experimental Results

The experimental parameters of the laser system used for this simulation are given in Table 3.1. Through the Fresnel integrals detailed in Section 2.6, an initial pulse was

Center wavelength	800 nm
Pulse length (FWHM)	35 fs
Initial beam width (FWHM)	11 mm
Aperture diameter	9 mm
Peak intensity in vacuum	6×10^{15} W/cm^2
Distance from aperture to lens	1.45 m
Lens focal length	1 m
Gas and pressure	He, 80 torr

Table 3.1 Experimental parameters

created that was used as the starting condition for the propagation code 5 cm before the nominal focus. A fluence profile of the propagation is shown in Fig. 3.1.

The results of the simulation show striking similarities to the experimental data. The pulse width exhibits minima at about 4 cm before and 3 cm after the nominal focus, as seen in the experimental data in Fig. 1.3. The intermediate region between the two minima in the simulation also has a flat-top radial profile, as observed by Painter [9]. A comparison of the FWHM profiles is shown in Fig. 3.2.

To further verify that the simulated pulse propagation corresponds to the actual propagation of the pulse, total ionization and energy lost to ionization were calculated. Fig. 3.3 is an ionization profile for the propagation region, which shows a long plasma streak, similar to what we observed visually in our experimental setup, with a peak ionization of about 2.5%. Experimental measurements were also made of the total energy lost to ionization, showing it to be less than 10% of the pulse energy (essentially negligible). Although the code does not attenuate the pulse energy as ionization occurs, the energy used for ionization can be calculated by summing the electron

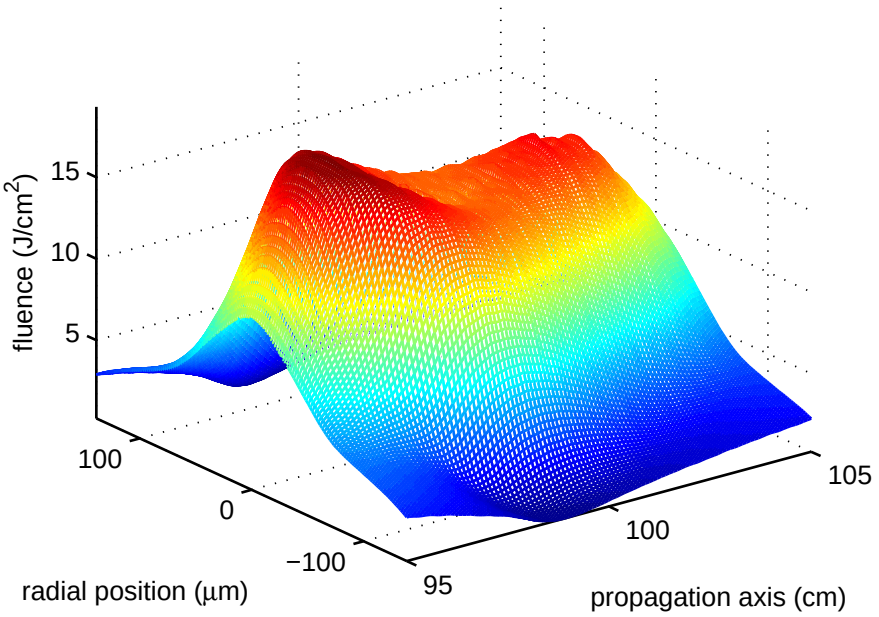

Figure 3.1 A fluence profile of the simulations results using the parameters given by Painter [9].

density to find the total number of ionized electrons and multiplying by the ionization potential plus the pondermotive energy. The calculated total amount of energy needed for ionization in the simulation turns out to be ∼4% of the total pulse energy, in agreement with experiment.

The spectral shift due to the effects of the generated plasma on the pulse can also be compared between simulation and experiment. At the nominal focus ($z = 100$ cm), Painter observed a blueshift of ∼4 nm on axis. A spectral profile can be calculated for the simulated data by applying a fast-Fourier transform to the electric field envelope, which gives a blueshift of ∼6 nm.

The simulation qualitatively agrees very well with experimental measurements, *i.e.*, features such as the two foci and the radial fluence flat-top profiles occur in the same regions, but there are small differences in quantitative results such as peak

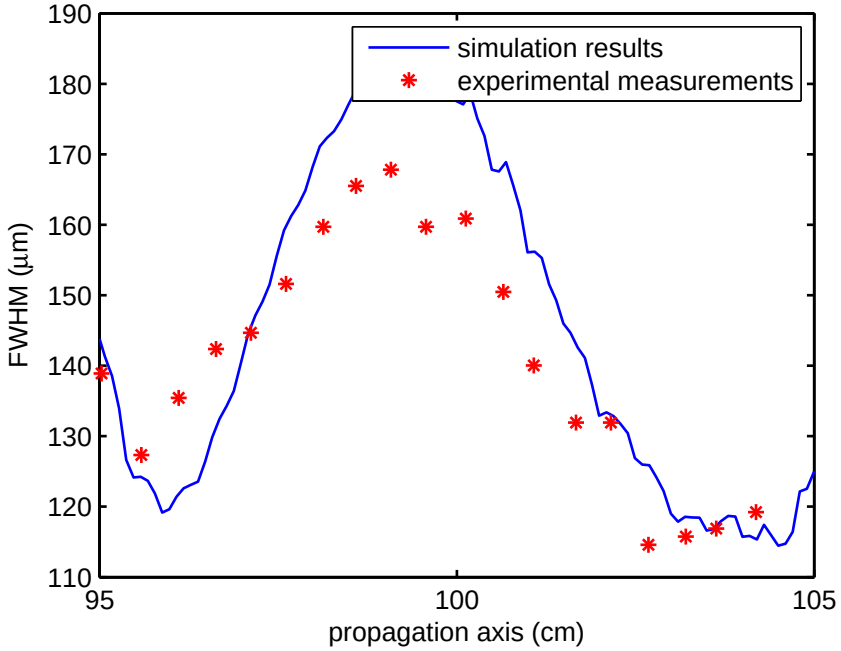

Figure 3.2 Fluence FWHM measurements from both experimental and simulated pulse propagation.

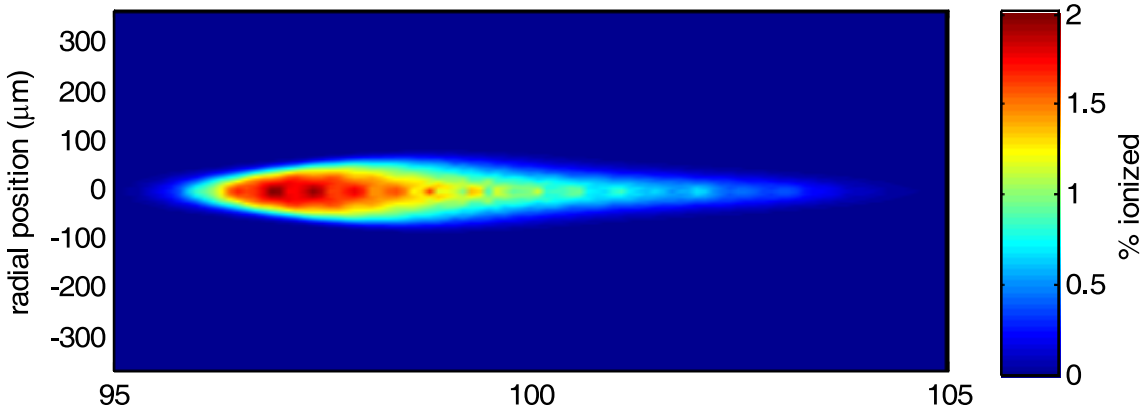

Figure 3.3 Calculated ionization for the region of propagation of the simulated pulse.

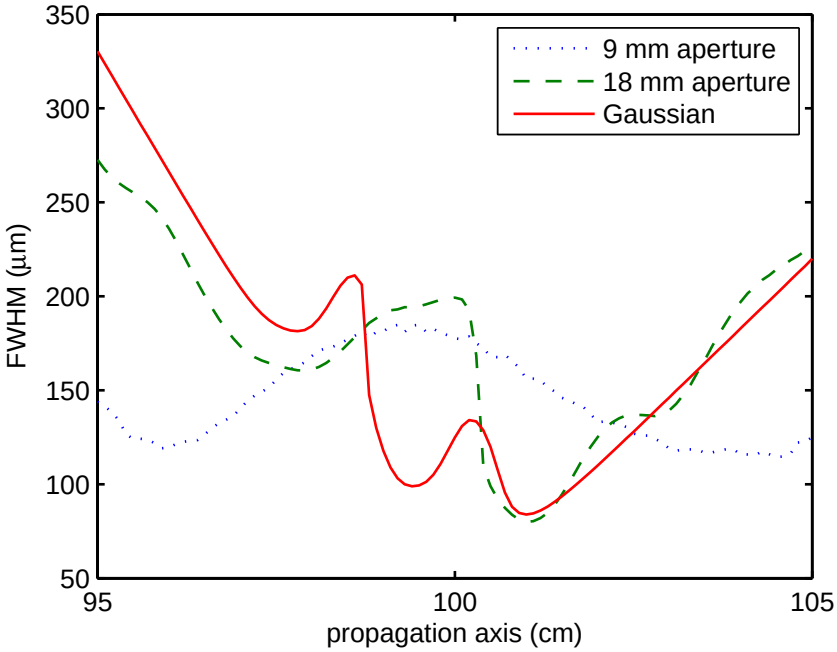

Figure 3.4 FWHM profiles for a unapertured Gaussian pulse and pulses apertured at diameters of 9 mm and 18 mm.

FWHM. We have observed that small variations in the parameters, such as the incoming beam width, the aperture diameter, and the pulse energy, can reduce these differences while staying within experimental uncertainties.

3.2 Analysis

To investigate the effect of an aperture, a unapertured Gaussian pulse and apertured pulses with diameters of 9 mm (the optimal diameter found by Painter) and 18 mm were propagated numerically from 5 cm before to 5 cm after the nominal focus. The FWHM profiles are shown in Fig. 3.4. As would be expected, the profile of the pulse with the 18 mm aperture closely resembles that of the unapertured Gaussian pulse. The fluctuations in the FWHM, due to the interaction between the pulse geometry and plasma generation, are markedly different for an unapertured and an

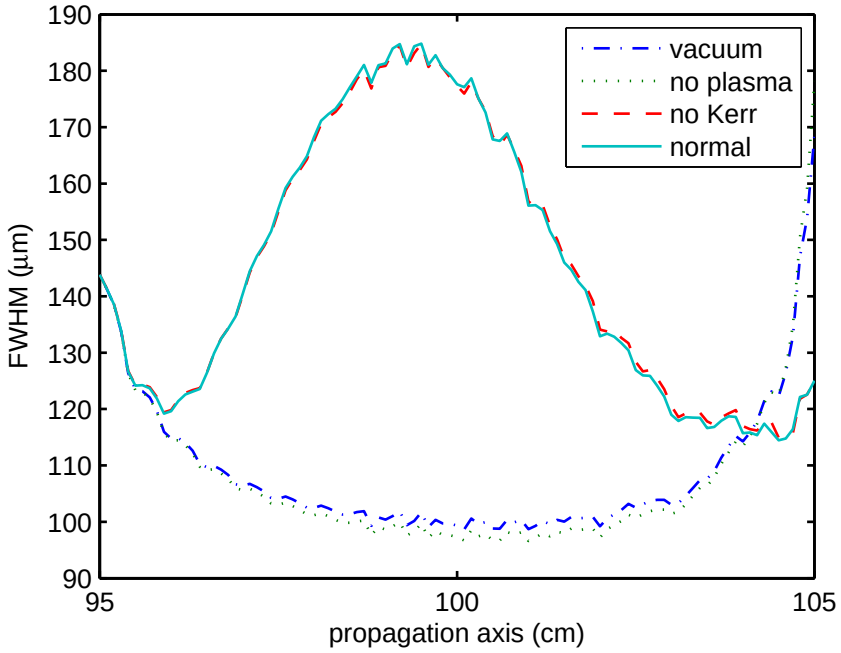

Figure 3.5 FWHM profiles for pulse propagation with and without plasma generation and the Kerr effect.

apertured pulse. The decreased aperture diameter causes the double focus profile we have observed experimentally. The complicated effects in the laser focus seen for the unapertured pulse are associated with the poor phase matching for high-harmonic generation.

The influence of the Kerr effect and plasma generation can also be observed by removing one or the other from the simulation. The FWHM profiles from these two cases, the normal simulation, and a simulation of the pulse in vacuum are shown in Fig. 3.5. As would be expected with our pulse power, Kerr self-focusing has little effect on the propagation of the pulse, even without plasma generation present. Defocusing of the pulse due to plasma generation causes the Kerr effect to have even less of an influence on the propagation of the pulse. The effect of the medium on the pulse propagation appears to be due entirely to plasma generation.

3.3 Conclusions

Our numerical simulations agree well with the experimental data with which we can compare our simulation, as demonstrated by Fig. 3.2. Owing to the extensive amount of agreement, we can conclude that our modeling is accurate and that the Kerr effect does not significantly influence on pulse propagation in our system. The observed phenomenon of the the dual foci is therefore not Kerr-style filamentation, which requires an appreciable value of $n_2 I$. Instead, the double focusing comes from plasma generation and the diffraction geometry from the aperture. This self-guiding [23] may be responsible for the good phase matching that gives rise to the experimentally-observed efficient harmonic generation. Investigation of the fluence profile and maximum intensities shows that the second waist actually has a lower intensity than the first waist. A plot of the peak intensity and peak fluence, shown in Fig. 3.6, shows that while the fluence has two local maxima, the intensity reaches a maximum at the first waist and then steadily decreases. The first waist corresponds to a peak in intensity as well as fluence, but the second waist is not a second focus in the ordinary sense. The intensity continually decreases along the direction of propagation in that region due to an increase in the pulse length.

3.4 Directions for Further Work

Although certain features of FWHM and pulse profiles such as self-guiding and a flat-top profile are associated with efficient high harmonic generation, the most direct way to predict good harmonic generation is to investigate phase matching. As explained in Chapter 1, small differences in the phase within the laser pulse can result in huge phase variations in the generated harmonic, causing destructive interference and low harmonic output. By determining the phase of each point in a snapshot of

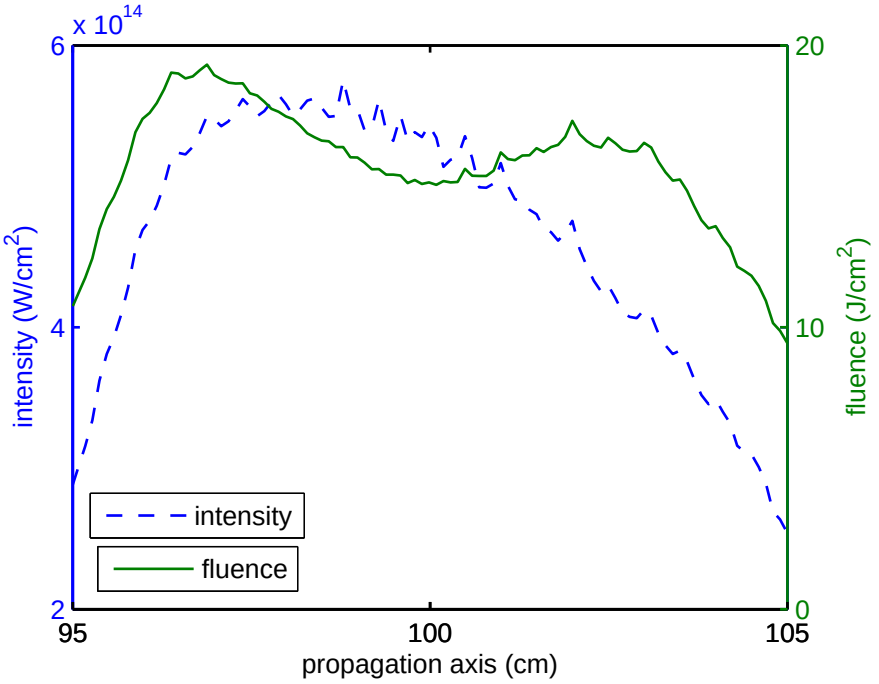

Figure 3.6 Calculated peak intensity and fluence for the simulated pulse propagation.

the electric field envelope, detailed maps of the phase variation from a plane wave can be produced. We plan to use this such phase maps to investigate and optimize phase matching in our setup. Experimentally, we have observed that variations in the aperture diameter and gas pressure can influence harmonic output. By using the simulation to predict harmonic generation efficiency, we will be able to investigate the influence of variations in these parameters, as well as other parameters, such as lens focal length. After we have optimized parameters in the simulation, we can modify our experimental setup accordingly, rather than making a series of modifications to our hardware to find optimal conditions.

Bibliography

[1] A. McPherson, G. Gibson, H. Jara, U. Johann, and T. S. Luk, "Studies of multiphoton production of vacuum-ultraviolet radiation in the rare gases," J. Opt. Soc. Am B **4,** 595–601 (1987).

[2] N. Brimhall, J. C. Painter, M. Turner, S. V. Voronov, R. S. Turley, M. Ware, and J. Peatross, "Construction of an extreme ultraviolet polarimeter based on high-order harmonic generation," In *Advances in X-Ray/EUV Optics, Components, and Applications. Edited by Khounsary, Ali M.; Morawe, Christian. Proceedings of the SPIE, Volume 6317, pp. 63170Y (2006).*, Presented at the Society of Photo-Optical Instrumentation Engineers (SPIE) Conference 6317 (2006).

[3] J. Sutherland, Master's thesis, Brigham Young University, 2005.

[4] J. B. Peatross, S. Voronov, and I. Prokopovich, "Selective zoning of high harmonic emission using counter-propagating light," Optics Express **1,** 114–125 (1997).

[5] S. Kazamias, F. Weihe, D. Douillet, C. Valentin, T. Planchon, S. Sebban, G. Grillon, F. Augé, D. Hulin, and P. Balcou, "High order harmonic generation optimization with an apertured laser beam," Eur. Phys. J. D **21,** 353–359 (2002).

[6] T. Liu, W. Lu, D. Wang, H. Yang, and Q. Gong, "Influence of circular aperture on high-order harmonic generation," Chin. Opt. Lett. **1,** 367–369 (2003).

[7] A. Chiron, G. Bonnaud, A. Dulieu, J. L. Miquel, G. Malka, M. Louis-Jacquet, and G. Mainfray, "Experimental observations and simulations on relativistic self-guiding of an ultra-intense laser pulse in underdense plasmas," Physics of Plasmas **3,** 1373–1401 (1996).

[8] C. Spielmann, C. Kan, N. H. Burnett, T. Brabec, M. Geissler, A. Scrinzi, M. Schnurer, and F. Krausz, "Near-keV coherent X-ray generation with sub-10-fs lasers," Ieee Journal of Selected Topics in Quantum Electronics **4,** 249–265 (1998), pT: J.

[9] J. Painter, Master's thesis, Brigham Young University, 2006.

[10] P. Béjot *et al.*, "32 TW atmospheric white-light laser," Applied Physics Letters **90,** 1106–+ (2007).

[11] A. Chiron, B. Lamouroux, R. Lange, J. F. Ripoche, M. Franco, B. Prade, G. Bonnaud, G. Riazuelo, and A. Mysyrowicz, "Numerical simulations of the non-linear propagation of femtosecond optical pulses in gases," Eur. Phys. J. D **6,** 383–396 (1999).

[12] F. Shimizu, "Numerical calculation. of self-focusing and trapping of a short light pulse in Kerr liquids," IBM J. Res. Dev. **17,** 286–298 (1973).

[13] M. Nurhuda, A. Suda, M. Hatayama, K. Nagasaka, and K. Midorikawa, "Propagation dynamics of femtosecond laser pulses in argon," J. Phys. D. **66,** 023811–+ (2002).

[14] M. D. Feit and J. A. Fleck, Jr., "Beam nonparaxiality, filament formation, and beam breakup in the self-focusing of optical beams," J. Opt. Soc. Am. B **5,** 633–640 (1988).

[15] D. J. Nicholas and S. G. Sajjadi, "Numerical simulation of filamentation in laser-plasma interactions ," J. Phys. D **19,** 737–749 (1986).

[16] J. Kasparian, J. Solle, M. Richard, and J.-P. Wolf, "Ray-tracing simulation of ionization-free filamentation," Appl. Phys. B **79,** 947–951 (2004).

[17] A. Brodeur, C. Y. Chien, F. A. Ilkov, S. L. Chin, O. G. Kosareva, and V. P. Kandidov, "Moving focus in the propagation of ultrashort laser pulses in air," Opt. Lett. **22,** 304 (1997).

[18] J. Sun and J. P. Longtin, "Effects of a gas medium on ultrafast laser beam delivery and materials processing," J. Opt. Soc. Am. B **21,** 1081–1088 (2004).

[19] P. Chernev and V. Petrov, "Self-focusing of light pulses in the presence of normal group-velocity dispersion," Opt. Lett. **17,** 172–174 (1992).

[20] S. Sartang, R. G. Evans, and W. T. Toner, "Numerical simulation of self-focusing in laser produced plasmas ," J. Phys. D **16,** 955–969 (1983).

[21] A. L'Huillier, P. Balcou, S. Candel, K. J. Schafer, and K. C. Kulander, "Calculations of high-order harmonic-generation processes in xenon at 1064 nm," Phys. Rev. A **46,** 2778–2790 (1992).

[22] E. Priori *et al.*, "Nonadiabatic three-dimensional model of high-order harmonic generation in the few-optical-cycle regime," Phys. Rev. A **61,** 063801–+ (2000).

[23] V. Tosa, E. Takahashi, Y. Nabekawa, and K. Midorikawa, "Generation of high-order harmonics in a self-guided beam," Phys. Rev. A **67,** 063817–+ (2003).

[24] E. Takahashi, V. Tosa, Y. Nabekawa, and K. Midorikawa, "Experimental and theoretical analyses of a correlation between pump-pulse propagation and harmonic yield in a long-interaction medium," Phys. Rev. A **68,** 023808–+ (2003).

[25] S. L. Chin, S. A. Hosseini, W. Liu, Q. Luo, F. Theberge, N. . Akozbek, A. Becker, V. P. Kandidov, O. G. Kosareva, and H. Schroeder, "The propagation of powerful femtosecond laser pulses in optical media: physics, applications, and new challenges," Canadian Journal of Physics **83,** 863–905 (2005).

[26] P. Chernev and V. Petrov, "Self-Focusing of Light-Pulses in the Presence of Normal Group-Velocity Dispersion," Opt. Lett. **17,** 172–174 (1992).

[27] J. Crank and P. Nicolson, "A Practical Method for Numerical Evaluation of Solutions of Partial Differential Equations of the Heat-Conduction Type," Proceedings of the Cambridge Philosophical Society **43,** 50–67 (1947).

[28] M. Ammosov, N. Delone, and V. Krainov, Sov. Phys. JETP **64,** 1191–1194 (1986).

Index